GSA DATA REPOSITORY 2018370 https://doi.org/10.1130/G45160.1

Ruohong Jiao, Frédéric Herman, Olivier Beyssac, Thierry Adatte, Simon C. Cox, Faye E. Nelson, Helen L. Neil

Erosion of the Southern Alps of New Zealand during the last deglaciation

Sediment core

Cruise TAN0712 was a research voyage programme led by National Institute of Water and Atmosphere (NIWA), with an aim to recover the late Quaternary glaciation history through the sedimentary records. A 2.65 m long (top lost) piston core TAN0712-27 (-43.753917°, 168.150617°) was recovered by RV *Tangaroa* from a submarine canyon levee at a water depth of 1369 m. The levee is composed of overspilled fine turbidity and hemipelagic sediment, with the bulk of terrestrial sediment entering the canyon system transported into the deep Tasman Sea (Neil et al., 2007). The core is described as olive grey homogeneous foram mud, with a gradational colour boundary to dark grey at 230 cm (Fig. DR1G) (Neil et al., 2007).

Environmental magnetic analysis

Volume-normalized magnetic susceptibility (κ) (SI; 0.1 sensitivity setting) and anhysteretic susceptibility (κARM) (saturation anhysteretic remanent magnetisation (ARM) normalized by applied bias field of 79.6 A/m) (Fig. DR1D) were measured at 1 cm resolution down-core on u-channels using a 2G Enterprises superconducting rock magnetometer with an inline AF demagnetizer, ARM solenoid and Bartington MS2 magnetic susceptibility loop meter at the University of Otago. Further rock magnetic experiments confirmed magnetite as the magnetic carrier in the TAN0712 cores (Nelson, 2011; Nelson et al., 2013). The major sources of magnetite in this part of the Southern Alps are metavolcanic horizons within the schist or exposures of the Dun Mountain Ultramafic Belt (Bradley et al., 2002). Magnetic susceptibility is a down-core parameter commonly used for correlation between cores; however, anhysteretic susceptibility records a significant signal in the TAN0712 cores post-LGM. Magnetic susceptibility is a measure of the concentration of diamagnetic, paramagnetic and, particularly, ferromagnetic (sensu lato) components. Multi-domain magnetite preferentially acquires magnetic susceptibility (κ), while single-domain magnetite

preferentially acquires anhysteretic susceptibility (κARM). Thus, κARM normalised by κ (Fig. DR1E) is a magnetic mineral grain-size proxy parameter (King et al., 1982). In this paper, the susceptibility signals are presented as a correlation tool. The climatic and oceanographic interpretations of the TAN0712-23 magnetite grain-size signal presented in Nelson et al. (2013) can also be applied to TAN0712-27. Broadly, quasi-concomitant fluctuation of κARM and κ (end of core to 225 cm; Figs. DR1D and E) is interpreted as a proxy for local glacier advance/stagnation during the LGM. This is followed by an interval of a low concentration of magnetite (225 to 187 cm) corresponding with glacier retreat and deglacial climate-oceanographic reorganization. An increased concentration of finer magnetite (187 cm to top of core) characterizes the Holocene.

Chronology and age model

Bulk planktic foraminifera were submitted by National Institute Water and Atmospheric Research (NIWA) and University of Otago for accelerator mass spectrometry (AMS) ^{14}C measurements at the Rafter National Isotope Centre, GNS Science. The radiocarbon ages were converted to calendar years BP (cal yr BP) using Calib 6.0 (Stuiver and Reimer, 2016) and the marine09.14c dataset (Reimer et al., 2016) (Table DR1). As described in Nelson et al. (2013), a regional reservoir correction age value of -35 was applied.

Here, the TAN0712-27 ^{14}C age model (Nelson, 2011) is further refined by tuning the anhysteretic and magnetic susceptibility ratio κARM/κ record to the ^{14}C dated TAN0712-23 (-44.037833°, 167.420667°) (Nelson et al., 2013) κARM/κ record using the spline interpolation function of AnalySeries 2.0 (Paillard et al., 1996), with a linear correlation of 0.96 (Table DR2; Fig. DR2).

Total Organic Carbon: tracer abundance in the source bedrocks and preservation of the tracer during the transfer to the ocean

Tracer abundance in the source rocks is a key parameter in provenance studies, as demonstrated by modelling in Nibourel et al. (2015). Here, Total Organic Carbon (TOC) in the source rocks represents the initial tracer abundance. We have compiled existing TOC data in the amphibolite, biotite, chlorite and sub-greenschist facies (prehnite-pumpellyite to pumpellyite-actinolite) schists/semischists in the Southern Alps, including data from single rocks (Hilton et al., 2008; Menzies et al., 2018) or river bedload material (Hilton et al., 2008; Horan et al., 2017; Nibourel et al., 2015). The *in situ* TOC measurements appear to show a general increase with the metamorphic grade, but show large variance for each type of rock,

indicating significant variation of carbon content at outcrop scale. Therefore, we follow Nibourel et al. (2015) and suggest that river bedload samples better represent the initial tracer abundance in the bedrock at the catchment scale. Using data from Nibourel et al. (2015), samples from rivers that drain mainly sub-greenschist rocks yield 0.06–0.09% TOC, indicating low carbon concentration. In catchments with chlorite and lower grade schist bedrocks, bedload samples yield 0.06–0.12% TOC, which increases to 0.1–0.16% if the catchments also comprise biotite schist rocks. Samples from catchments with no sub-greenschist rocks present higher TOC content of 0.17–0.18%. These observations imply a slightly lower carbon content in the chlorite schist than that in the biotite schist, although an accurate estimate is difficult due to the spatially varying erosion of bedrocks in a single catchment. Therefore, for this paper we impose a ratio in the range of 0.6–1.0 for the TOC ratio between chlorite and biotite schist, and consider it to be able to account for the uncertainty in tracer abundance in the source rocks.

We have also analysed total carbon content for new bedload material in the main rivers draining our region of interest, and for comparison, samples of Nibourel et al. (2015) from Whataroa River (Table DR4). The analyses were carried out using a CHN Elemental Analyzer (Carlo 184 Erba Flash EA 1112 CHNS/MAS200) on ~10 mg of dry powdered sediment. The precision was better than 1% based on an internal standard, and replicate samples. The reanalysed Whataroa samples show a good agreement with the TOC measurements obtained by Nibourel et al. (2015), who used a different analytical procedure. From the results, we observe that the bedload samples from the southwest of the Southern Alps, from our region of interest, show a smaller variation in the carbon content than that further north. For example, samples from Cascade, Arawhata, Waiatoto and Haast yield a small range of total carbon content of 0.076–0.115, despite the catchments containing schist bedrock in very different proportions of metamorphic grade. We interpret this as being due to rocks in the southwest belonging almost entirely within the Aspiring Lithologic Association with very similar primary sedimentological characteristics but different degrees of metamorphism (Rattenbury et al., 2010). In contrast catchments in the northeast (e.g., Whataroa) contain a primary sedimentological boundary with lithostratigraphic variation parallel to the metamorphic isograds that is reflected locally in a variation in TOC (Nibourel et al., 2015). This further validates our selection of a wide range of TOC ratios between chlorite and biotite schists (0.6–1.0), sufficient to cover the potential variation in the tracer abundance in source rocks in the study area.

Another important point is the possible weathering of rock-derived carbon material (CM) affecting TOC all along the pathway from bedrock to the marine sediments. If significant weathering is occurring, it could bias the provenance tool towards the CM of highest peak temperatures (>500–550°C) as the more disordered CM corresponding to lower peak temperatures are more prone to weathering (e.g., Galy et al., 2008; Bouchez et al., 2010). In the Southern Alps, we have assumed that weathering is negligible, based on the observation of a lack of bias towards higher temperature carbonaceous material, i.e., the >550°C high temperatures are actually poorly represented in our detrital RSCM data. Moreover, from the cold, dry LGM to the warm, humid Holocene, the increasing proportion of CM of low peak temperatures suggests insignificant impact from weathering on the distribution of CM peak temperatures.

Such weathering of CM is important in large scale erosional systems like the Himalayas to Bengal Fan (Galy et al., 2008) or the Andes-Amazon (Bouchez et al., 2010) systems, and carbon budgets show that the oxidation of rock-derived CM occurs in the large floodplains where sediments are stored over long periods. In a small-scale system like Taiwan based on a similar approach for carbon budget, Hilton et al. (2011) estimated a global oxidative flux of rock-derived CM up to 15% ± 7%, which likely affects immature and reactive CM sourced from very low grade metamorphic rocks present in this mountain belt and likely happens in soils (Hemingway et al., 2018). First, we note that CM in the Southern Alps is composed by graphitic carbon as it was submitted to metamorphism of peak temperatures generally higher than 300°C (Beyssac et al., 2016). All the labile fraction of organic carbon, which is prone to oxidative weathering, has been released from these rocks during burial, and the remaining graphitic carbon is highly, though not completely, refractory to bio-chemical weathering.

However, we acknowledge that in small-scale active mountain belts like the Southern Alps or Taiwan, recent studies using rhenium as a proxy for CM oxidation show that a fraction of rock-derived CM is lost during weathering in soils or glacial colluviums (Hilton et al., 2014; Horan et al., 2017), which is further confirmed by a budget of the oxidation of rock-derived CM in soils from Taiwan based on isotopic and organic geochemistry (Hemingway et al. 2018). In the Southern Alps, soils and glacial colluviums are thin (Horan et al., 2017; Larsen et al., 2014), and we assume their contribution to bedload material in rivers and marine sediments to be negligible compared to that of rocks excavated during landslide activity. Therefore, considering that rock-derived CM travels mostly in the river bedload compared to the suspended load (Galy et al., 2008), we assume that, as previously

justified by Hilton et al. (2014) and Horan et al. (2017), the TOC in river bedload is representative of TOC in the source rocks. In addition, in the Southern Alps, the transport in rivers and the subsequent turbidity deposition in the canyon are efficient and rapid, and therefore we expect no further weathering of rock-derived OC in such small-scale erosional system comparable what was described in Taiwan (Hilton et al., 2011; Kao et al., 2014). Altogether, we assume that the contribution of weathering of rock-derived CM, if any, remains lower than the uncertainty of the TOC inherited from the source rock lithology.

Raman spectroscopy of carbonaceous material (RSCM) thermometry

RSCM thermometry is based on quantification of the degree of graphitization of CM, which is a reliable indicator of metamorphic temperature (T). Because of the irreversible character of graphitization, CM structure is not sensitive to the retrograde path during exhumation of rocks and records the maximum T reached during metamorphism in the range 330–640°C (Beyssac et al., 2002) or even at lower temperature (Lahfid et al., 2010). Here Raman microspectroscopy is used to compare the structure of rock-derived fossil organic carbon in the marine sediments to that of fossil organic carbon in the mountain bedrocks. We convert the Raman parameters describing the degree of graphitization into peak metamorphic temperatures using the equations provided by Beyssac et al. (2002) and Lahfid et al. (2010).

Raman analysis of the marine sediments was performed directly on the sample raw powder without any chemical or mechanical extraction thus preserving the pristine structure of fossil organic carbon. Raman spectra were obtained by point measurement mapping using a Renishaw InVia Reflex instrument. This system is equipped with a Leica DMLM microscope, a grating with 1800 grooves per millimeter and a charge-coupled device detector. Spectra were excited using the 514.5 nm emission line of an argon laser (<1 mW measured at the sample surface) with a circular polarization thanks to a quarter wavelength plate set in the optical path before the microscope. We used a Leica objective x50 (numerical aperture of 0.75) that yields a planar resolution of nearly 1 μm. The spectral resolution of the system is estimated at around 1.5 cm^{-1} in the configuration used. Wavenumber calibration was done using a silicon standard and Ne lamp emission. On each sample, we collected 185–228 spectra to have statistically significant data. To complement the dataset provided by Beyssac et al. (2016) in the source region of sediments, 16 new thin-sections of bedrock samples were analyzed using the same Raman spectrometer and following strictly the analytical procedure described by Beyssac et al. (2016). All Raman spectra from sediments and bedrocks (including those from Beyssac et al., 2016) were then fitted following the procedure

described in Beyssac et al. (2002), Lahfid et al. (2010) and using the software provided by Sparkes et al. (2013). We noted that the temperatures of some CM of ~350–370 °C could be underestimated to <330 °C in the automated peak fitting procedure using five Lorentz peaks, and therefore these spectra are manually selected and estimated using three Voigt peaks. This manual correction affects <5% measurement in our sediment samples, and ~1% in the bedrock dataset. Table DR3 provides RSCM T value for each single spectrum obtained per marine sediment and new bedrock sample.

X-ray Diffraction mineralogy

XRD analyses were conducted on bulk rock for all the samples at the Institute of Earth Sciences the University of Lausanne, Switzerland. The samples were prepared following the procedure of Adatte et al. (1996) and Kübler (1983). Random powder of the bulk sample is used for characterization of the whole rock mineralogy. About 20 g of material from each rock sample was ground with a "jaw" crusher to obtain small chips (1 to 5 mm). Approximately 5 g of material was dried at 60°C and then ground to a homogenous powder with particle sizes <40 µm. About 800 mg of this powder was pressed (20 bars) in a powder holder covered with a blotting paper and analyzed by XRD. Whole rock composition was determined by XRD (Thermo ARL X'TRA Diffractometer, Switzerland) based on methods previously described (Klug and Alexander, 1974; Kübler, 1983; Rolli, 1990). This method uses external standards for semi-quantitative analysis of the bulk rock mineralogy, which were obtained by XRD patterns of random powder samples.

Clay mineral analyses were based on methods described by (Kübler, 1983). Ground chips were mixed with de-ionized water (pH 7–8) and agitated. The carbonate fraction was removed with the addition of 10% HCl (1.25 N) at room temperature for 20 minutes, or until all the carbonate was dissolved. Ultrasonic disaggregation was accomplished during 3 minutes intervals. The insoluble residue was washed and centrifuged (5–6 times) until a neutral (pH 7–8) suspension was obtained. Separation of different grain size fractions (< 2µm and 2–16 µm) was obtained by the timed settling method based on the Stokes law. The selected fraction was then pipetted onto a glass plate. XRD analyses of oriented clay samples were made after air-drying at room temperature and ethylene-glycol solvated conditions. The intensities of selected XRD peaks were measured to obtain a semi-quantitative estimate of their corresponding clay minerals (e.g., chlorite, mica, kaolinite, palygorskite, sepiolite, smectite and illite-smectite mixed-layers) in the size-fractions < 2µm and 2–16µm. Therefore,

clay minerals are given in relative percent abundance without correction factors. Content in swelling (% smectite) is estimated by using the method of Moore and Reynolds (1989).

Detrital provenance model

We assume that in the sediment sample, the fraction of CM from upper amphibolite facies schist is c_1, garnet amphibolite schist c_2, biotite schist c_3, chlorite schist c_4 and sub-greenschist facies semischist c_5, where $\sum_{i=1}^{5} c_i = 1$. Therefore, the cumulative distribution function (CDF) of RSCM temperature in a sediment sample is predicted as

$$CDF_p = \sum_{i=1}^{5} (c_i \cdot CDF_i)$$

where CDF_i is the CDF of RSCM temperature in each provenance, which is estimated from the bedrock data (Fig. DR4). The cumulative distribution function of observed RSCM temperature is CDF_o. The goodness of fit between CDF_p and CDF_o is estimated using the Kolmogorov-Smirnov test, and is optimized by minimizing the K-S statistic using a Markov Chain Monte Carlo method. A total of 200,000, including 100,000 burn-in, iterations were run for each sample. Fig. DR5 shows the model results.

Potential variation of the source area

The core is from a submarine canyon levee and the dominant deposits are 1) overspilling of fine sediments from turbidity currents and 2) hemipelagic sedimentation. The bulk of sediment eroded locally from the Southern Alps is transported within the canyon to the deep ocean. In this setting, we do not think the longshore drift or other ocean surface currents have an effect on the sediment transport to the core. Near the core site, the surface water most likely flows predominantly towards the south or southwest (Fig. DR6). If the surface currents play a role in transporting sediments to the core, the Holocene sediments would have more CM of high temperature (>500°C or even 600°C) from the central Southern Alps than the LGM sediments, which contradicts our observations.

Alternatively, the effect of Coriolis force on the overspill sediments is more considerable, and therefore it may be possible for the core to also receive some overspill sediments from the Moeraki Canyon, which is connected to the Haast, Okuru, and Turnbull catchments as well as river systems further north (Fig. 1). However, as the distribution of biotite and chlorite schist rocks in these rivers follow a similar pattern to the Waiatoto and Arawhata rivers (i.e. increasing metamorphic grade from the mountain front to upper valleys), including them as source areas should not change our conclusion. To test this point of view,

we predict the potential erosion intensity of a source area including the Haast, Okuru, Turnbull, Waiatoto and Arawhata catchments, following the same procedure described in DISCUSSION in the main text. The predicted erosion patterns from these catchments due to fluvial incision, glacial abrasion and large landslides are shown in Fig. DR8, respectively. The calculated CS-sediment proportions differ by 1–8% from models using only Waiatoto and Arawhata catchments, due to the varying area proportions of the schist rocks outcropped in the Haast, Okuru, Turnbull catchments vs. Waiatoto and Arawhata catchments. However, the general trend does not change: the relative contribution from chlorite schist sediments is higher in materials eroded by landslides than that by glacial erosion and fluvial incision. Therefore, including a larger area in the Southern Alps as the provenance does not change our conclusions.

Table DR1 Radiocarbon ages from core TAN0712-27.

Table DR2 Age constraints for TAN0712-27.

Table DR3 RSCM temperature data from the marine sediments in the Waiatoto Canyon and the bedrock samples from the Waiatoto and Arawhata catchments.

Table DR4 New total carbon measurements using a CHN analyzer.

Table DR5 Compiled total organic carbon measurements from the Southern Alps, including single rock data from biotite, chlorite and sub-greenschist facies schist/semischist rocks and river bedload data from catchments draining these bedrocks.

Fig. DR1 (A) X-ray diffraction mineralogy of bulk sediments. Circles indicate depths for RSCM samples. (B) X-ray diffraction mineralogy of clay minerals. (C) Distribution of RSCM temperature data from selected sediment samples. (D) Magnetic susceptibility and anhysteretic susceptibility. (E) Magnetic grain size (κARM/κ). (F) Colour reflectance. (G) Photograph of the core.

Fig. DR2 Age model of TAN0712-27, correlated to TAN0712-23 using anhysteretic and magnetic susceptibility ratio κARM/κ.

Fig. DR3 Quartz content and quartz/feldspar ratios measured in sand samples from rivers in western Southern Alps, based on X-ray diffraction bulk mineralogy. Grey shades depict results in the canyon sediments from core TAN0712-27.

Fig. DR4 Distributions of bedrock RSCM temperature data from the Southern Alps, shown as probability (histogram) and cumulative density functions (curve). Data are from Beyssac et al. (2016) and from this study (see Table DR3).

Fig. DR5 Mixture models of detrital RSCM temperature data from TAN0712-27 sediments. Observed probability (histogram) and cumulative density functions (curve) are shown in blue, and predicted cumulative density functions are shown as red curves. *P*-value and c_{pi} represent the mean post-burn-in models; c_{p1}–c_{p5} indicate proportion of materials from upper amphibolite schist, garnet amphibolite schist, biotite schist, chlorite schist and sub-greenschist facies semischist, respectively.

Fig. DR6 Directions of dominant ocean currents off the west coast of South Island. Small arrows are mean surface currents from 1992 to 1996, which are calculated from a near real-time model (Ocean Surface Current Analysis Real-time) from NASA (1/3-degree and 5-day resolution). Large arrows are taken from Carter et al. (1998).

Fig. DR7 Predicted erosion intensity distribution in the Waiatoto and Arawhata catchments by different processes. Erosion intensity is predicted for each 75-m cell, and normalized to the maximum value of each model. (upper) Fluvial erosion intensity predicted by a digital elevation model resampled from the SRTM data, using the unit stream power law, $\varepsilon=A^{0.5}S$ (Finlayson et al., 2002). Map is coloured by averaging the initial ε with a 525 m-wide square kernel. (middle) Glacial erosion intensity predicted by a LGM icefield model (Golledge et al., 2012) using a quadratic function, $\varepsilon=\mu^2$ (Herman et al., 2015). (lower) Landslide erosion calculated from an inventory of landslides with large (affecting area A>0.2 km^2) landslides (Heron, 2014), using a volume–area scaling factor of 1.5, i.e. $V=A^{1.5}$ (Hovius et al., 1997; Larsen et al., 2010). TopoToolbox (Schwanghart and Scherler, 2014) was used for calculation and creating figures.

Fig. DR8 Same as Fig. DR7, but for a larger source area including Waiatoto, Arawhata, Turnbull, Okuru and Haast-Landsborough catchments.

References

Adatte, T., Stinnesbeck, W., and Keller, G., 1996, Lithostratigraphic and mineralogic correlations of near K/T boundary clastic sediments in northeastern Mexico: Implications for origin and nature of deposition: Geological Society of America Special Papers, v. 307, p. 211-226.

Beyssac, O., Cox, S. C., Vry, J., and Herman, F., 2016, Peak metamorphic temperature and thermal history of the Southern Alps (New Zealand): Tectonophysics, v. 676, p. 229-249.

Beyssac, O., Goffé, B., Chopin, C., and Rouzaud, J. N., 2002, Raman spectra of carbonaceous material in metasediments: a new geothermometer: Journal of Metamorphic Geology, v. 20, no. 9, p. 859-871.

Bouchez, J., Beyssac, O., Galy, V., Gaillardet, J., France-Lanord, C., Maurice, L., and Moreira-Turcq, P., 2010, Oxidation of petrogenic organic carbon in the Amazon floodplain as a source of atmospheric CO2: Geology, v. 38, no. 3, p. 255-258.

Bradley, J. P., Chew, P. M., and Wilkins, C. J., 2002, Transport and distribution of magnetite and ilmenite on Westland beaches of New Zealand; with comment on the accumulation of other high‐density minerals: Journal of the Royal Society of New Zealand, v. 32, no. 1, p. 169-181.

Carter, L., Garlick, R., Sutton, P., Chiswell, S., Oien, N., and Stanton, B., 1998, Ocean circulation New Zealand, National Institute of Water and Atmosphere Chart Miscellaneous Series, Volume 76.

Finlayson, D. P., Montgomery, D. R., and Hallet, B., 2002, Spatial coincidence of rapid inferred erosion with young metamorphic massifs in the Himalayas: Geology, v. 30, no. 3, p. 219-222.

Galy, V., Beyssac, O., France-Lanord, C., and Eglinton, T., 2008, Recycling of Graphite During Himalayan Erosion: A Geological Stabilization of Carbon in the Crust: Science, v. 322, no. 5903, p. 943-945.

Golledge, N. R., Mackintosh, A. N., Anderson, B. M., Buckley, K. M., Doughty, A. M., Barrell, D. J. A., Denton, G. H., Vandergoes, M. J., Andersen, B. G., and Schaefer, J. M., 2012, Last Glacial Maximum climate in New Zealand inferred from a modelled Southern Alps icefield: Quaternary Science Reviews, v. 46, p. 30-45.

Hemingway, J. D., Hilton, R. G., Hovius, N., Eglinton, T. I., Haghipour, N., Wacker, L., Chen, M.-C., and Galy, V. V., 2018, Microbial oxidation of lithospheric organic carbon in rapidly eroding tropical mountain soils: Science, v. 360, no. 6385, p. 209-212.

Herman, F., Beyssac, O., Brughelli, M., Lane, S. N., Leprince, S., Adatte, T., Lin, J. Y. Y., Avouac, J.-P., and Cox, S. C., 2015, Erosion by an Alpine glacier: Science, v. 350, no. 6257, p. 193-195.

Heron, D. W., 2014, Geological Map of New Zealand 1:250 000: GNS Science, scale 1:250,000.

Hilton, R. G., Gaillardet, J., Calmels, D., and Birck, J.-L., 2014, Geological respiration of a mountain belt revealed by the trace element rhenium: Earth and Planetary Science Letters, v. 403, no. Supplement C, p. 27-36.

Hilton, R. G., Galy, A., and Hovius, N., 2008, Riverine particulate organic carbon from an active mountain belt: Importance of landslides: Global Biogeochemical Cycles, v. 22, no. 1, p. GB1017.

Hilton, R. G., Galy, A., Hovius, N., Horng, M.-J., and Chen, H., 2011, Efficient transport of fossil organic carbon to the ocean by steep mountain rivers: An orogenic carbon sequestration mechanism: Geology, v. 39, no. 1, p. 71-74.

Horan, K., Hilton, R. G., Selby, D., Ottley, C. J., Gröcke, D. R., Hicks, M., and Burton, K. W., 2017, Mountain glaciation drives rapid oxidation of rock-bound organic carbon: Science Advances, v. 3, no. 10.

Hovius, N., Stark, C. P., and Allen, P. A., 1997, Sediment flux from a mountain belt derived by landslide mapping: Geology, v. 25, no. 3, p. 231-234.

Kao, S. J., Hilton, R. G., Selvaraj, K., Dai, M., Zehetner, F., Huang, J. C., Hsu, S. C., Sparkes, R., Liu, J. T., Lee, T. Y., Yang, J. Y. T., Galy, A., Xu, X., and Hovius, N., 2014, Preservation of terrestrial organic carbon in marine sediments offshore Taiwan: mountain building and atmospheric carbon dioxide sequestration: Earth Surf. Dynam., v. 2, no. 1, p. 127-139.

King, J., Banerjee, S. K., Marvin, J., and Özdemir, Ö., 1982, A comparison of different magnetic methods for determining the relative grain size of magnetite in natural materials: Some results from lake sediments: Earth and Planetary Science Letters, v. 59, no. 2, p. 404-419.

Klug, H. P., and Alexander, L. E., 1974, X-Ray Diffraction Procedures: For Polycrystalline and Amorphous Materials, 2nd Edition, New York, John Wiley & Sons, Inc.

Kübler, B., 1983, Dosage quantitatif des minéraux majeurs des roches sédimentaires par diffraction X, Cahiers de l'Institut de Géologie Neuchâtel, Série AX N°1.1 &1.2.

Lahfid, A., Beyssac, O., Deville, E., Negro, F., Chopin, C., and Goffé, B., 2010, Evolution of the Raman spectrum of carbonaceous material in low-grade metasediments of the Glarus Alps (Switzerland): Terra Nova, v. 22, no. 5, p. 354-360.

Larsen, I. J., Almond, P. C., Eger, A., Stone, J. O., Montgomery, D. R., and Malcolm, B., 2014, Rapid Soil Production and Weathering in the Southern Alps, New Zealand: Science, v. 343, no. 6171, p. 637-640.

Larsen, I. J., Montgomery, D. R., and Korup, O., 2010, Landslide erosion controlled by hillslope material: Nature Geosci, v. 3, no. 4, p. 247-251.

Menzies, C. D., Wright, S. L., Craw, D., James, R. H., Alt, J. C., Cox, S. C., Pitcairn, I. K., and Teagle, D. A. H., 2018, Carbon dioxide generation and drawdown during active orogenesis of siliciclastic rocks in the Southern Alps, New Zealand: Earth and Planetary Science Letters, v. 481, no. Supplement C, p. 305-315.

Moore, D. M., and Reynolds, R. C., 1989, X-ray Diffraction and the Identification and Analysis of Clay Minerals, Oxford, Oxford University Press.

Neil, H., Mitchell, J., Wilcox, S., Gerring, P., Bostock, H., and Northcote, L., 2007, West Coast Canyons 2 (TAN0712) NIWA voyage report (10 September–4 October 2017): Wellington, New Zealand, National Institute of Water and Atmospheric Research.

Nelson, F. E., 2011, Paleomagnetic records of the last two million years of climate and oceanographic change in the New Zealand sector of the South Pacific [PhD thesis]: University of Otago, 256 p.

Nelson, F. E., Wilson, G. S., and Neil, H. L., 2013, Marine magnetic signature of the Last Glacial Maximum and last deglaciation from the Southern Hemisphere mid-latitudes: Marine Geology, v. 346, p. 246-255.

Nibourel, L., Herman, F., Cox, S. C., Beyssac, O., and Lavé, J., 2015, Provenance analysis using Raman spectroscopy of carbonaceous material: A case study in the Southern Alps of New Zealand: Journal of Geophysical Research: Earth Surface, v. 120, no. 10, p. 2015JF003541.

Paillard, D., Labeyrie, L., and Yiou, P., 1996, Macintosh Program performs time-series analysis: Eos, Transactions American Geophysical Union, v. 77, no. 39, p. 379-379.

Reimer, P. J., Baillie, M. G. L., Bard, E., Bayliss, A., Beck, J. W., Blackwell, P. G., Bronk Ramsey, C., Buck, C. E., Burr, G. S., Edwards, R. L., Friedrich, M., Grootes, P. M., Guilderson, T. P., Hajdas, I., Heaton, T. J., Hogg, A. G., Hughen, K. A., Kaiser, K. F., Kromer, B., McCormac, F. G., Manning, S. W., Reimer, R. W., Richards, D. A., Southon, J. R., Talamo, S., Turney, C. S. M., van der Plicht, J., and Weyhenmeyer, C. E., 2016, IntCal09 and Marine09 Radiocarbon Age Calibration Curves, 0–50,000 Years cal BP: Radiocarbon, v. 51, no. 4, p. 1111-1150.

Rolli, M., 1990, Dosage semi-quantitatif RX sur Scintag, Cahiers de l'Institut de Géologie de Neuchâtel, Suisse, Série ADX, p. 1-49.

Schwanghart, W., and Scherler, D., 2014, Short Communication: TopoToolbox 2 – MATLAB-based software for topographic analysis and modeling in Earth surface sciences: Earth Surf. Dynam., v. 2, no. 1, p. 1-7.

Sparkes, R., Hovius, N., Galy, A., Kumar, R. V., and Liu, J. T., 2013, Automated Analysis of Carbon in Powdered Geological and Environmental Samples by Raman Spectroscopy: Applied Spectroscopy, v. 67, no. 7, p. 779-788.

Stuiver, M., and Reimer, P. J., 2016, Extended 14C Data Base and Revised CALIB 3.0 14C Age Calibration Program: Radiocarbon, v. 35, no. 1, p. 215-230.

Figure DR1

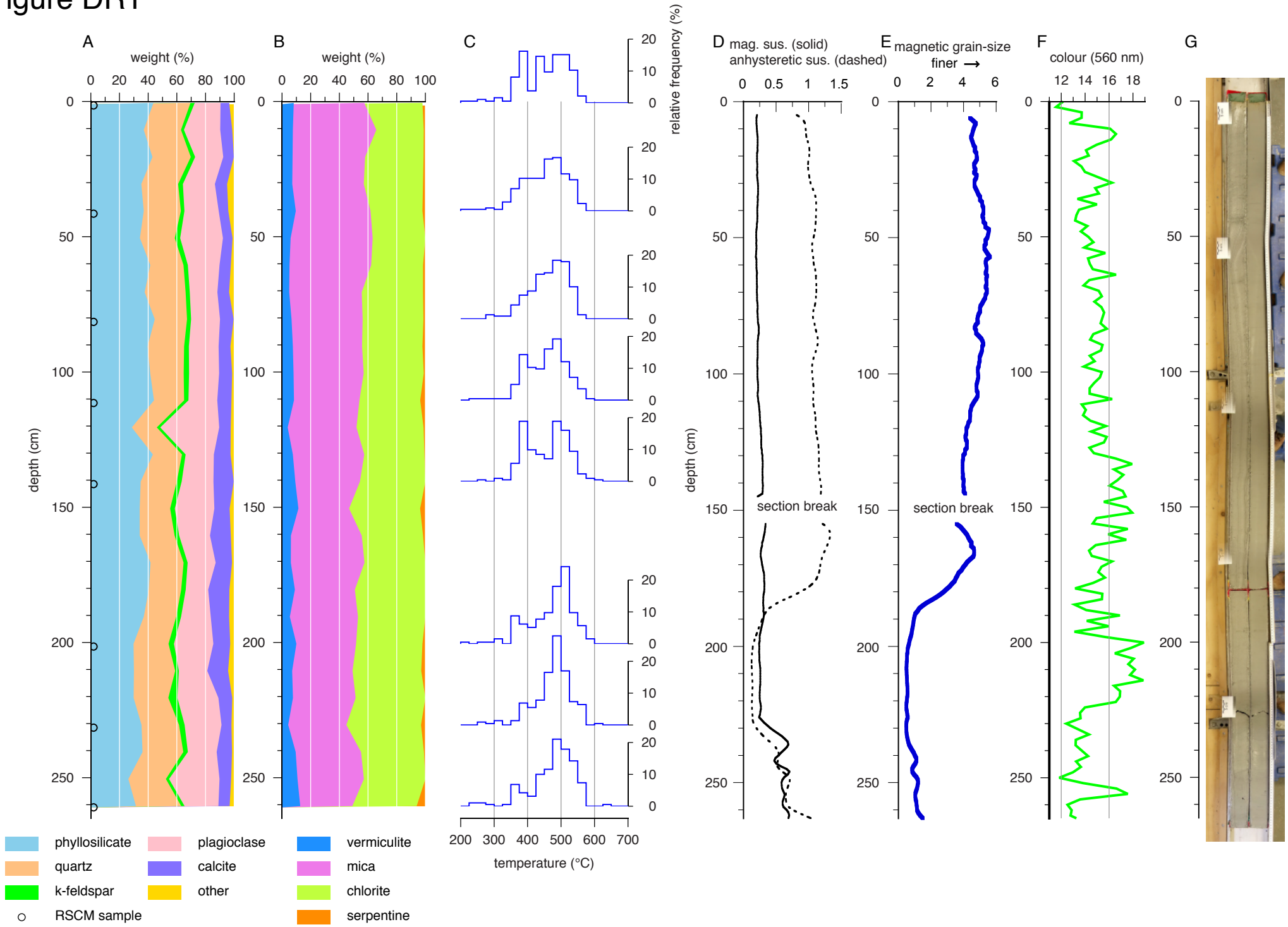
A
weight (%)
0 20 40 60 80 100
B
weight (%)
0 20 40 60 80 100
C
relative frequency (%)
temperature (°C)
200 300 400 500 600 700
D mag. sus. (solid)
anhysteretic sus. (dashed)
0 0.5 1 1.5
E magnetic grain-size
finer →
0 2 4 6
F
colour (560 nm)
12 14 16 18
G
depth (cm)
0 50 100 150 200 250
section break
section break
phyllosilicate
quartz
k-feldspar
RSCM sample
plagioclase
calcite
other
vermiculite
mica
chlorite
serpentine

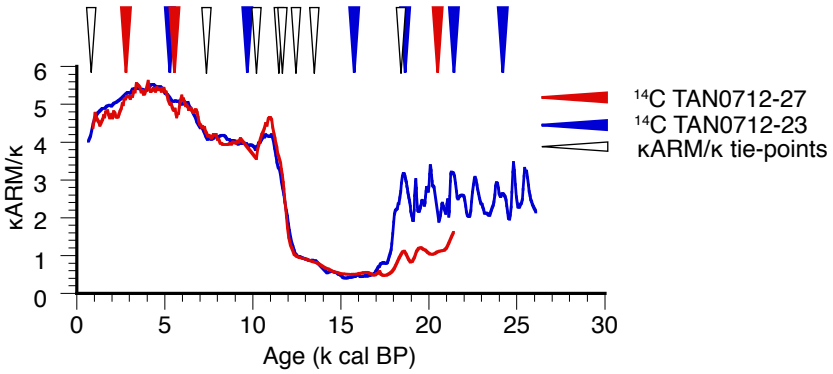
6
5
4
3
2
1
0
κARM/κ
0
5
10
15
20
25
30
Age (k cal BP)
14C TAN0712-27
14C TAN0712-23
κARM/κ tie-points

Figure DR2

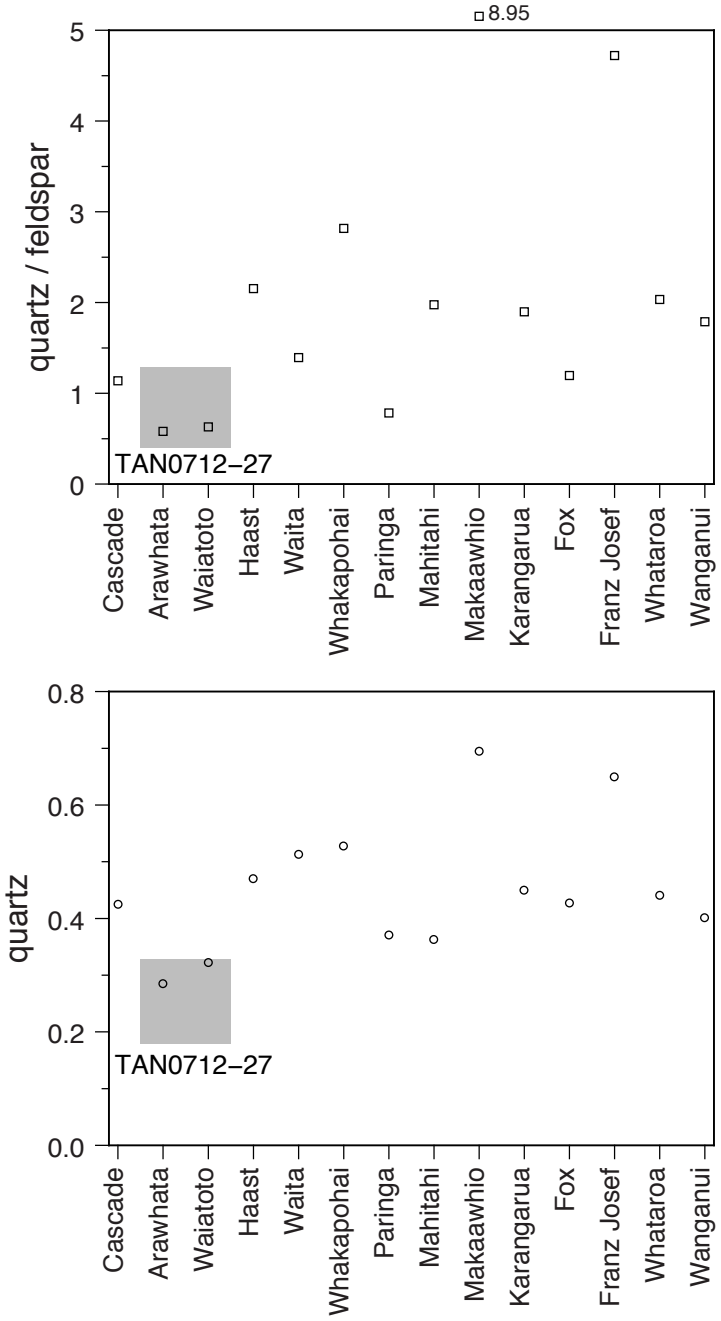
quartz / feldspar
8.95
TAN0712–27
quartz
TAN0712–27
Cascade
Arawhata
Waiatoto
Haast
Waita
Whakapohai
Paringa
Mahitahi
Makaawhio
Karangarua
Fox
Franz Josef
Whataroa
Wanganui

Figure DR3

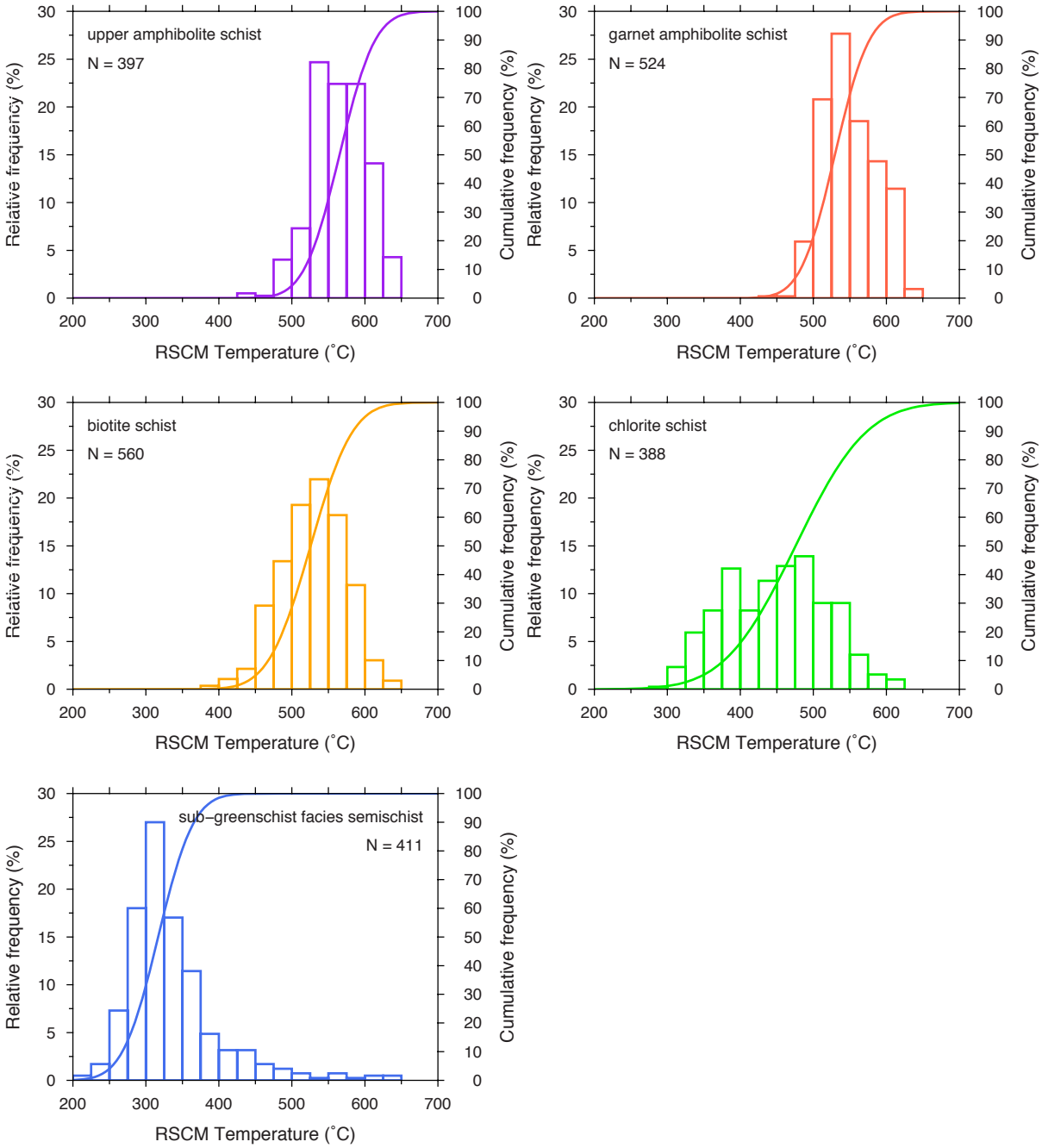
upper amphibolite schist
N = 397
garnet amphibolite schist
N = 524
biotite schist
N = 560
chlorite schist
N = 388
sub–greenschist facies semischist
N = 411
Relative frequency (%)
Cumulative frequency (%)
RSCM Temperature (˚C)

Figure DR4

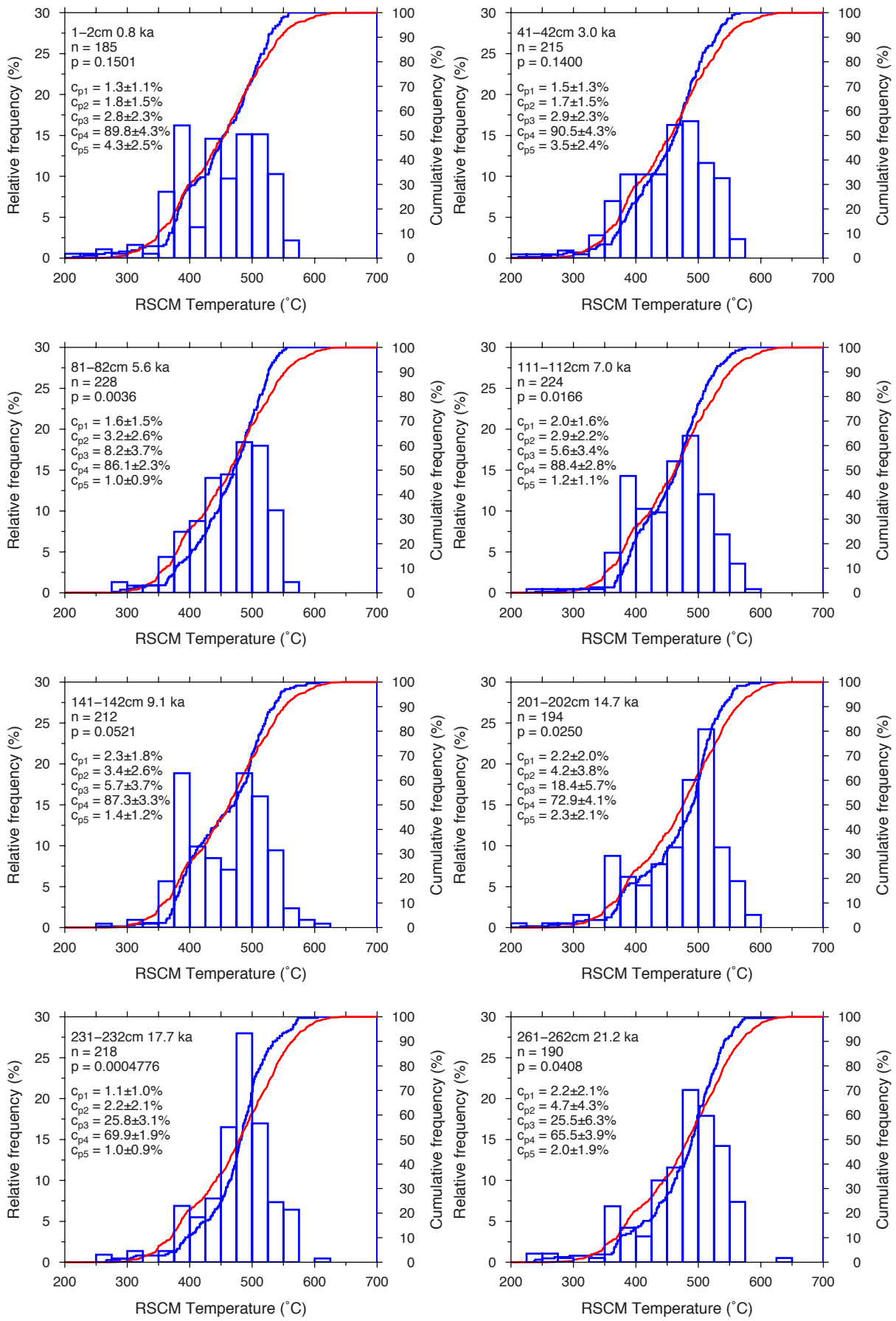
1–2cm 0.8 ka
n = 185
p = 0.1501
c_{p1} = 1.3±1.1%
c_{p2} = 1.8±1.5%
c_{p3} = 2.8±2.3%
c_{p4} = 89.8±4.3%
c_{p5} = 4.3±2.5%
41–42cm 3.0 ka
n = 215
p = 0.1400
c_{p1} = 1.5±1.3%
c_{p2} = 1.7±1.5%
c_{p3} = 2.9±2.3%
c_{p4} = 90.5±4.3%
c_{p5} = 3.5±2.4%
81–82cm 5.6 ka
n = 228
p = 0.0036
c_{p1} = 1.6±1.5%
c_{p2} = 3.2±2.6%
c_{p3} = 8.2±3.7%
c_{p4} = 86.1±2.3%
c_{p5} = 1.0±0.9%
111–112cm 7.0 ka
n = 224
p = 0.0166
c_{p1} = 2.0±1.6%
c_{p2} = 2.9±2.2%
c_{p3} = 5.6±3.4%
c_{p4} = 88.4±2.8%
c_{p5} = 1.2±1.1%
141–142cm 9.1 ka
n = 212
p = 0.0521
c_{p1} = 2.3±1.8%
c_{p2} = 3.4±2.6%
c_{p3} = 5.7±3.7%
c_{p4} = 87.3±3.3%
c_{p5} = 1.4±1.2%
201–202cm 14.7 ka
n = 194
p = 0.0250
c_{p1} = 2.2±2.0%
c_{p2} = 4.2±3.8%
c_{p3} = 18.4±5.7%
c_{p4} = 72.9±4.1%
c_{p5} = 2.3±2.1%
231–232cm 17.7 ka
n = 218
p = 0.0004776
c_{p1} = 1.1±1.0%
c_{p2} = 2.2±2.1%
c_{p3} = 25.8±3.1%
c_{p4} = 69.9±1.9%
c_{p5} = 1.0±0.9%
261–262cm 21.2 ka
n = 190
p = 0.0408
c_{p1} = 2.2±2.1%
c_{p2} = 4.7±4.3%
c_{p3} = 25.5±6.3%
c_{p4} = 65.5±3.9%
c_{p5} = 2.0±1.9%
Relative frequency (%)
Cumulative frequency (%)
RSCM Temperature (˚C)

Figure DR5

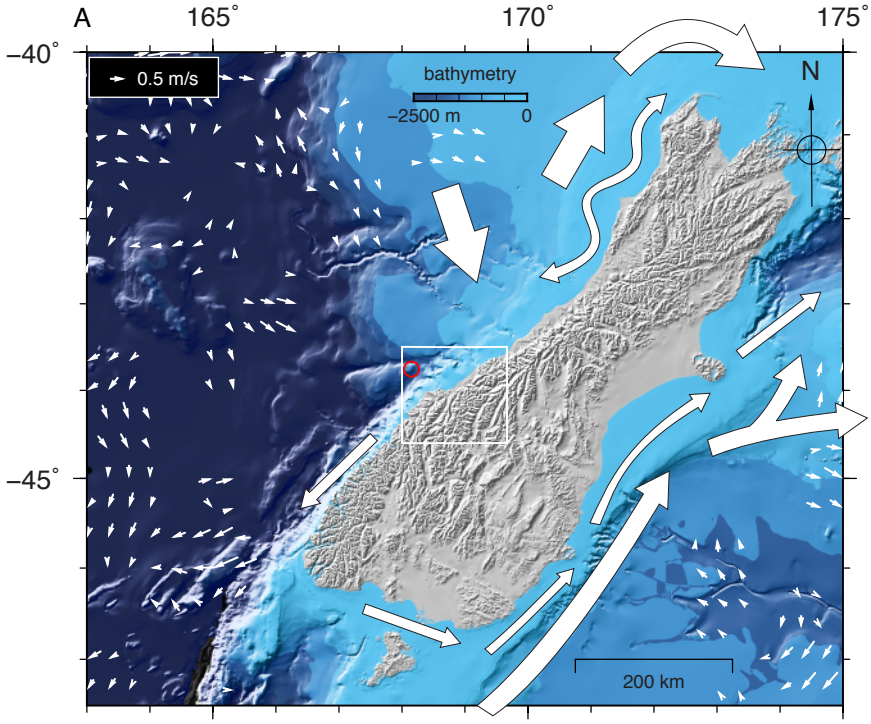

Figure DR6

Fluvial incision

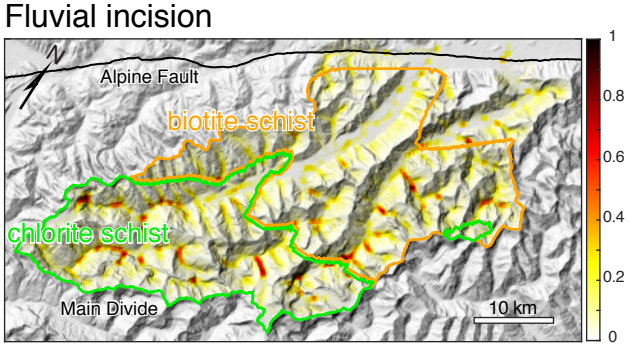

Glacial abrasion

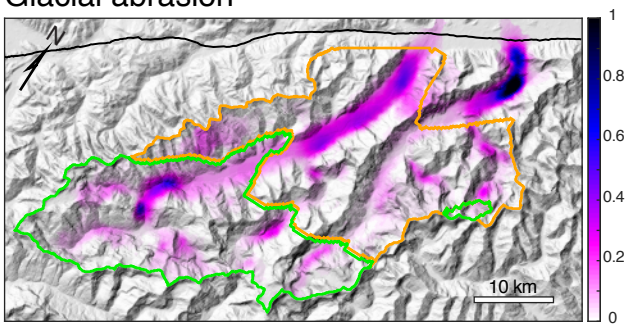

Large landslides

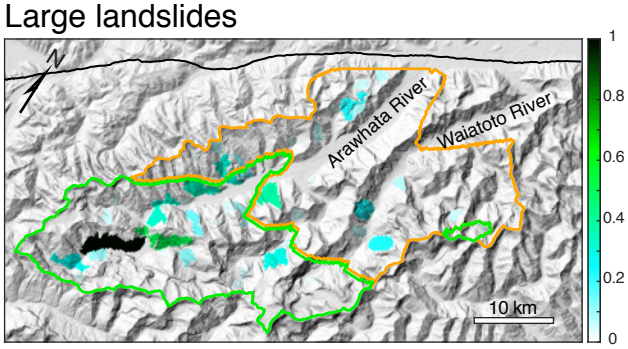

Figure DR7

Fluvial incision

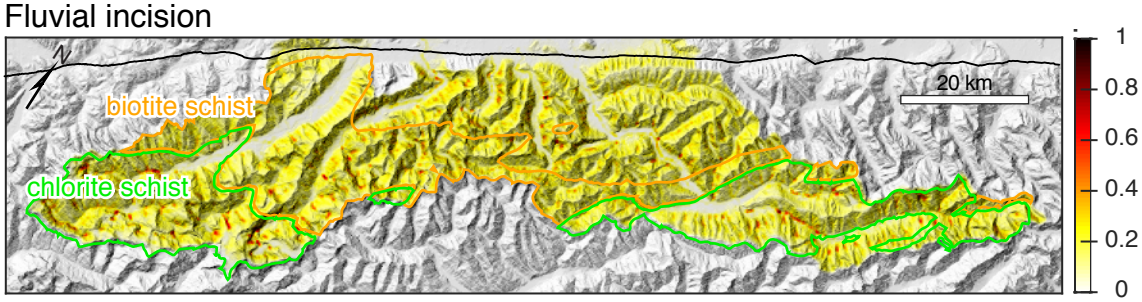

Glacial abrasion

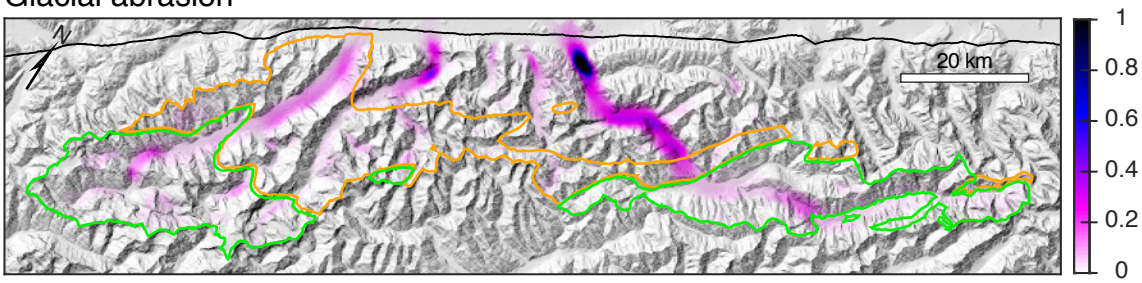

Large landslides

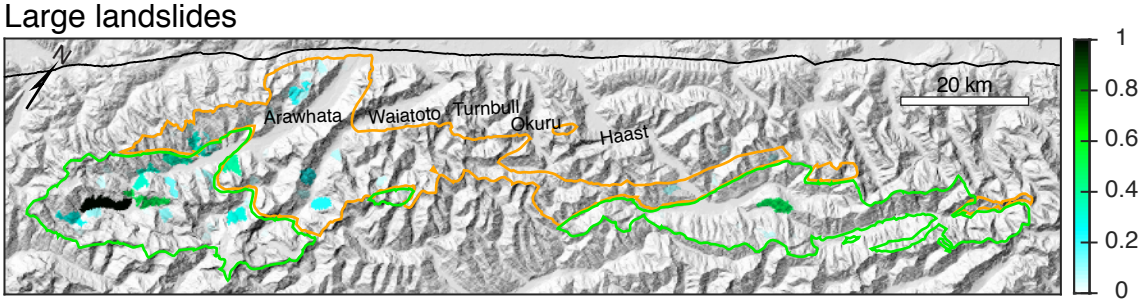

Figure DR8

Table DR1 Radiocarbon ages from core TAN0712-27

Depth (cm)	Lab number	Age (year BP)	Calibrated age (cal BP)*
40-41	NZA33190	3114±58	2940 (2780:3110)
80-80.5	NZA33191	5164±58	5560 (5440:5680)
259-259.5	NZA33679	17804±75	20770 (20380:21210)

*Median probability. Ages in parentheses are the 2σ age range.

Table DR2 Age model for TAN0712-27

Depth (cm)	Age (k cal BP)	Tie-point
6.23	0.946	Tuning (κARM/κ)
40.5	2.938	AMS
80.5	5.56	AMS
120	7.441	Tuning (κARM/κ)
154.67	10.173	Tuning (κARM/κ)
173.17	11.441	Tuning (κARM/κ)
180.5	11.793	Tuning (κARM/κ)
188.47	12.402	Tuning (κARM/κ)
194.7	13.541	Tuning (κARM/κ)
241.7	18.541	Tuning (κARM/κ)
259.25	20.767	AMS

Table DR3

RSCM temperature (°C) of the core sediments

TAN0712-27-1-2 cm

445	373	534	449	505	489	364	320	487	557	367	231	455	538	414	494	438	523	489	253	506	493	479	307	393
388	451	462	373	397	435	412	388	527	376	411	425	545	450	509	425	462	471	373	386	503	547	481	474	409
382	525	368	525	472	437	443	497	485	478	453	475	435	388	514	430	436	363	366	498	496	364	382	265	492
504	511	499	319	358	548	213	476	440	432	528	449	466	451	330	381	375	381	500	382	441	481	458	526	514
399	432	366	488	520	512	527	507	438	545	488	532	541	486	523	373	501	362	525	559	389	402	391	461	465
559	547	380	408	434	390	376	504	434	441	375	453	462	519	524	432	388	381	387	475	504	527	481	534	520
376	391	462	520	448	437	418	510	511	488	502	537	490	487	485	446	383	378	380	550	532	490	450	457	399
509	385	483	366	475	393	288	514	434	506															

TAN0712-27-41-42 cm

471	387	535	464	435	362	492	413	506	392	506	506	496	423	476	497	284	367	377	533	440	433	459	412	476
473	477	415	385	501	364	481	473	326	482	522	537	343	438	425	442	374	418	444	468	448	408	456	540	424
449	528	485	490	427	528	467	404	389	474	250	485	508	547	488	451	462	377	474	497	361	471	405	389	498
503	531	461	468	527	559	500	411	497	489	413	505	458	493	448	487	370	370	485	503	377	436	528	482	433
555	401	536	364	337	445	386	491	476	399	412	389	475	290	453	427	469	409	413	466	367	536	459	529	524
478	523	501	441	462	471	327	507	464	374	362	461	457	538	473	374	472	478	534	382	431	374	435	318	482
264	376	501	450	384	513	339	393	546	488	511	439	547	454	515	508	465	502	501	487	487	486	424	512	455
482	445	336	213	484	467	454	363	371	440	486	543	419	473	546	478	388	461	393	402	395	511	378	488	391
495	411	527	422	566	555	418	384	517	404	474	506	554	525	384										

TAN0712-27-81-82 cm

415	462	411	525	496	379	448	375	288	329	404	518	494	543	541	303	538	425	421	507	521	401	383	488	525
500	524	451	490	441	474	530	504	470	452	440	466	373	492	432	490	531	411	503	432	520	525	312	542	551
449	517	379	417	464	471	486	461	464	532	365	417	526	488	362	518	428	510	424	446	524	450	364	549	367
433	449	495	436	511	458	411	521	528	480	545	470	522	363	276	510	440	527	371	470	510	504	451	402	376
364	549	384	512	389	364	381	421	521	513	522	428	290	502	483	489	556	492	331	483	509	400	491	500	433
539	540	489	367	500	509	510	489	469	426	503	421	554	405	507	450	459	455	402	430	482	490	475	482	457
469	510	464	486	447	444	448	376	395	477	451	469	454	431	499	414	391	495	433	486	412	402	527	466	511
376	478	465	525	427	478	480	491	462	504	496	496	489	473	502	428	526	435	392	378	446	484	527	487	522
513	517	470	459	439	439	451	473	520	489	533	449	470	396	419	482	535	518	409	500	535	450	530	378	476
461	496	484																						

TAN0712-27-111-112 cm

413	456	482	504	387	444	439	454	367	542	481	453	507	420	329	547	400	490	391	482	576	499	513	509	528
490	541	473	471	491	391	517	485	529	513	413	472	478	488	393	418	476	394	498	398	418	433	402	392	475
472	371	419	465	380	559	495	473	531	437	416	492	371	367	547	476	483	525	488	485	551	450	438	470	464
401	446	442	468	413	494	504	392	378	371	447	566	483	371	365	571	423	402	515	413	536	509	492	543	460
436	483	511	457	508	480	555	460	482	546	433	400	387	552	499	380	473	447	395	471	391	454	439	395	491
380	239	515	436	379	382	393	466	512	441	478	508	502	498	535	465	508	272	394	386	473	462	432	446	366
289	414	497	399	406	454	441	521	450	522	403	378	531	486	526	529	422	499	395	388	465	497	514	475	450
473	465	527	513	491	312	445	369	370	459	406	384	497	467	476	551	388	521	408	487	519	367	491	480	468
526	460	501	448	376	559	420	382	388	476	507	389	517	464	483	437	426	478	461	481	503	497	401	401	

TAN0712-27-141-142 cm

375	412	508	467	522	561	489	519	434	370	414	364	434	464	464	547	536	383	391	452	518	478	406	396	513
511	403	384	571	542	446	506	450	500	495	524	445	484	385	373	496	493	363	375	510	446	376	391	522	384
362	538	496	423	501	502	458	413	535	395	494	483	371	436	380	398	494	498	588	528	395	440	396	254	487
474	491	482	522	494	504	496	519	477	420	427	494	551	504	434	545	514	368	491	521	457	418	483	516	474
312	498	539	497	416	499	506	568	402	478	473	368	385	537	478	303	497	496	535	376	503	471	399	512	377
505	442	445	525	388	376	508	465	498	525	553	479	483	499	449	537	411	394	494	371	543	476	516	433	451
434	410	372	455	387	532	517	449	507	491	587	545	525	384	487	464	381	403	383	500	509	546	399	546	499
379	510	517	387	389	478	542	511	395	422	608	390	429	425	424	410	389	404	400	328	379	364	376	385	529
390	402	428	377	522	525	491	396	368	473	408	408													

TAN0712-27-201-202 cm

557 524 368 508 543 464 555 452 545 215 463 370 484 500 514 369 531 378 365 513 519 518 504 502 494
535 479 374 510 513 542 531 425 498 504 354 489 498 482 534 301 468 406 499 559 438 445 563 520 371
519 488 495 497 582 506 454 521 510 496 471 551 459 517 445 562 353 577 418 504 382 522 502 551 471
384 522 384 505 508 467 519 500 527 463 445 506 554 444 526 376 363 554 514 448 534 384 365 494 509
470 469 488 488 422 373 482 444 455 533 495 485 509 504 503 528 539 477 556 462 505 450 431 405 361
401 543 498 500 496 389 512 306 498 599 486 497 468 459 488 497 374 547 509 514 538 469 278 520 409
490 511 492 377 376 378 526 448 520 483 493 506 532 478 443 374 505 361 515 507 432 407 513 481 444
370 425 509 319 381 261 390 405 418 372 451 475 426 476 538 497 556 416 523

TAN0712-27-231-232 cm

389 387 461 311 419 501 481 470 486 446 498 411 314 497 441 433 498 526 498 574 566 482 306 498 479
366 484 473 485 362 503 551 457 510 480 440 489 514 485 490 544 504 431 505 493 517 443 485 472 462
493 454 540 398 473 544 454 492 491 447 571 459 504 569 500 496 472 509 494 516 409 534 477 510 498
498 530 469 426 378 559 486 572 435 549 477 502 469 498 379 394 440 501 410 501 451 476 477 489 266
504 490 573 490 514 531 455 391 449 484 566 485 412 438 521 503 385 562 475 451 466 548 499 449 523
416 464 456 422 518 479 380 449 384 470 476 475 495 480 533 438 520 515 521 484 405 436 492 410 417
457 567 566 497 494 513 485 497 527 540 458 461 487 526 506 477 458 488 524 571 468 462 416 468 384
368 501 481 459 605 478 502 464 452 517 523 403 533 481 468 512 478 467 537 477 533 520 483 473 469
502 459 487 486 508 475 398 433 502 268 288 394 556 390 384 473 494 507

TAN0712-27-261-262 cm

469 496 396 364 457 460 488 371 502 509 490 518 432 437 508 510 502 503 498 449 472 453 434 554 448
442 491 524 528 494 555 510 521 467 534 483 626 491 368 526 531 533 514 513 427 556 434 397 486 425
428 568 484 372 523 550 384 329 574 457 555 480 537 409 541 571 536 519 486 496 554 466 498 511 503
558 503 497 518 535 558 521 564 518 533 516 374 508 565 365 498 424 461 270 497 568 509 542 375 450
499 496 492 482 457 488 513 375 510 480 540 481 458 368 495 478 404 514 542 438 410 411 467 397 477
463 365 444 361 489 521 489 544 530 529 497 535 251 571 480 532 494 491 477 366 371 377 470 522 531
463 365 526 485 510 448 392 295 520 498 494 463 239 541 237 435 432 525 470 467 532 512 543 533 461
548 467 489 437 393 459 501 434 434 528 487 499 450 503 412

RSCM temperature (°C) of bedrock samples

Amphibolite schist

P75155 (44.03164°S 168.89564°E)

568 596 498 487 601 538 510 603 616 537 634 564 559 569 590 606 478 525 586 536

P76018 (44.09621°S 168.79659°E)

587 609 573 610 607 603 542 607 579 533 533 612 530 596 527 641 612 561 544 535

P76021 (44.08364°S 168.78685°E)

556 606 523 582 540 544 558 586 515 526 617 513 525 518 511 537 501 509 508 489 504

P77769 (44.08872°S 168.91525°E)

601 599 559 527 577 559 591 573 583 511 579 536 552 553 581 544 530 557 560 542

Biotite schist

P27180 (44.26104°S 168.67378°E)

469 535 529 524 563 510 498 487 505 496 482 479 512 493 493 494 479 497 497 534 535

P52513 (44.2768°S 168.47067°E)

541 524 508 598 561 499 583 587 595 571 532 600 540 600 520 574 505 540 572 503

P52526 (44.36843°S 168.42218°E)

562 462 593 550 563 547 590 527 529 539 556 519 575 515 530 545 460 555 569 492 570 568

P52829 (44.33024°S 168.43644°E)

549 535 610 613 560 539 613 545 575 575 547 561 509 534 525 561 554 606 554 535

P73977 (44.12632°S 168.69438°E)

574 499 492 558 596 573 497 534 544 565 552 588 542 593 565 504 511 582 533

P75097 (44.20826°S 168.56231°E)

513 587 562 569 586 521 510 595 572 545 585 573 577 571 569 592 572 509 426 575

P75118 (44.21634°S 168.77971°E)

494 542 511 498 554 550 500 505 543 485 495 534 485 551 484 513 557 496 492 510

P77710 (44.17081°S 168.87013°E)

528 556 575 541 495 549 528 539 525 552 546 576 552 542 589 516 501 533 476 559

Chlorite schist

P27701 (44.38362°S 168.7226°E)

535 550 494 480 509 477 489 519 466 539 509 538 542 520 498 508 513 482 586 491

P52528 (44.38265°S 168.35899°E)

459 474 537 516 559 484 478 452 487 495 466 490 457 497 485 477 477 484 490 463

P71679 (44.49452°S 168.35256°E)

435 425 451 433 426 438 429 421 430 392 432 442 437 429 459 408 440 428 444 444 431

P71725 (44.40705°S 168.41887°E)

435 449 478 443 412 466 464 453 433 461 464 453 447 444 446 434 438 475 424 466

Table DR4 New total carbon (C), nitrogen (N), and hydrogen (H) measurements

Sample	Catchment	Latitude (°)	Longitude (°)	Main metamorphic grades	Weight (mg)	N (%)	C (%)	H (%)
STD CYS1					5.093	11.640	30.000	5.050
WAT2*	Whataroa	-43.37707	170.42199	chlorite, low**	22.184	0.006	0.108	0.307
WAT3*	Whataroa	-43.40932	170.41643	chlorite, low	34.246	0.000	0.101	0.324
WAT7*	Whataroa	-43.40861	170.41249	chlorite, low	25.755	0	0.199	0.292
WAT8*	Whataroa	-43.44470	170.37691	chlorite, low	24.309	0	0.096	0.305
WAT9*	Whataroa	-43.31520	170.41983	garnet	23.954	0	0.248	0.243
WAT10*	Whataroa	-43.29308	170.41361	higher, garnet, biotite, chlorite, low	21.195	0	0.135	0.249
WAT11*	Whataroa	-43.18746	170.44983	higher, garnet	23.500	0	0.156	0.255
WAT14*	Whataroa	-43.34733	170.49040	biotite, chlorite, low	18.086	0	0.151	0.277
WAT15*	Whataroa	-43.34240	170.52947	biotite, chlorite	22.634	0	0.210	0.305
WAT16*	Whataroa	-43.37560	170.57091	low	22.525	0	0.062	0.256
STD CYS2					3.565	10.881	30.053	5.498
WAT17*	Whataroa	-43.37668	170.57071	low	23.368	0	0.068	0.292
WAT19*	Whataroa	-43.31045	170.31362	higher, garnet	20.827	0	0.220	0.222
P85585	Cascade	-44.10571	168.51996	chlorite, low	23.444	0	0.076	0.253
P85587	Arawhata	-44.04614	168.72346	biotite, chlorite	21.803	0	0.090	0.209
P85588	Waitoto	-43.98954	168.79799	biotite	24.925	0	0.115	0.204
P85589	Haast	-43.85488	169.04595	higher, garnet, biotite, chlorite, low	22.994	0	0.099	0.184
P85590	Waita	-43.78998	169.12229	higher	22.453	0	0.137	0.177
P85591	Whakapohai	-43.72940	169.24537	higher	22.128	0	0.132	0.303
P85592	Paringa	-43.70589	169.48746	higher, garnet, biotite, chlorite	22.378	0	0.126	0.190
STD CYS3					4.509	11.147	30.172	4.684
P85593	Mahitahi	-43.63468	169.58406	higher, garnet, biotite, chlorite	23.491	0	0.116	0.175
P85594	Makaawhio	-43.57638	169.68512	higher, garnet, biotite	22.680	0	0.154	0.151
P85595	Karangarua	-43.57419	169.80583	higher, garnet, biotite, chlorite	24.292	0	0.174	0.193
STD CYS4					5.268	11.277	30.352	5.842

*Samples from Nibourel et al. (2015) are reanalysed.

**Sub-greenschist facies.